VLASS Project Memo #14:

Correction of position errors in mosaic images without w-term corrections

M. Lacy (NRAO)

December 17, 2021

VLASS images made using the mosaic gridder suffer from systematic positional offsets $\lesssim 1$ arcsec. In this Memo, we show that these offsets are a result of neglecting the w-terms in the imaging algorithm. We show that the magnitude of these offsets depend only on the zenith distance of the observation, scaled with an amplitude related to the effective size of the S-band primary beam. We further show that a simple correction applied to the centers of the VLASS image products can reduce these errors to $< 1/10$ of the VLASS synthesized beam width (0.3 arcsec) over the whole survey, and to < 0.2 arcsec above Decl. -30°. The variation of the offsets with the square of the wavelength adds a further complication for wideband data. For VLASS, we show that these effects on the synthesized beam are small ($\lesssim 2\%$ of the peak) for tt0 images, but for tt1 (and thus spectral index images derived from them) the effects can be large ($\Delta\alpha \approx 0.2$). We recommend that VLASS cube images use a frequency dependent position correction to correctly align cube planes for derivation of accurate spectral indices.

1. Introduction

The positional accuracy of sources in radio interferometric images is determined by a number of factors. At the center of a single pointing, the accuracy is determined by the

accuracy of the position of the phase calibrator and the quality of the phase referencing. Further out in the primary beam, wide-field effects become important and will typically dominate the positional error budget (e.g. Bracewell et al. 1984). VLASS was designed to use on-the-fly mosaicking, and the effects of wide-field terms on the positional accuracy had not been quantified for this observing mode prior to the start of the survey. We therefore used a combination of *Gaia* Early Data Release 3 (EDR3) data (*Gaia* collaboration et al. 2016; *Gaia* Collaboration et al. 2020) and the rfc_2020d version of the VLBI radio fundamental catalog (RFC; Petrov et al. 2021 and refs. therein; `http://astrogeo.org/rfc/`) to check the accuracy of the VLASS positions.

The *Gaia* EDR3 contains high quality, sub-milliarcsecond precision astrometry for more than 1 billion objects. Gaia positions are accurate to $<<$ 1 mas, and Gaia sources detected in VLASS (nearly all quasars) are dense enough on the sky (234592 matches to VLASS within 1.5 arcsec, ~ 4 per square degree) that a meaningful test of systematic positional offsets can be carried out. The RFC is a compilation of several surveys, mostly with the VLBA, designed to provide a dense reference system of highly-accurate (milliarcsecond) astrometry for both astronomical and geodesic applications. The catalog lists over 18000 objects (≈ 0.5 per square degree, with 16791 sources matched to VLASS within 1.5 arcsec). Differences between VLBI and *Gaia* positions are very small compared to the VLASS beam (at most tens of mas, Kovalev et al. 2017), and are ascribed to physical offsets in the emission regions close to the black hole in AGN. They thus will average to zero within a large sample.

We first matched the *Gaia* catalog against a preliminary version of the VLASS Quick Look component list (most of these matches are quasars or nearby galaxies). The results of this match showed systematic offsets at the sub-arcsecond level between VLASS and *Gaia* that were a function of Declination and the Hour Angle of the VLASS observation (Figure 1). We subsequently confirmed these offsets with the RFC. In this memo, we use the comparison to *Gaia* and VLBI astrometry to show that neglect of wide-field terms in the Quick Look imaging algorithm leads to systematic positional offsets in mosaic images that are detectable in the VLASS image products, model these effects, and describe the correction that was made to the Quick Look and mosaic-gridded Single Epoch (SE) images that removes the bulk of this offset.

2. Analysis

Consider an observation of the sky made in a direction corresponding to the unit vector $\mathbf{s} = (\alpha, \delta)$, where α is the Right Ascension and δ the Declination. Using the standard conventions, let $\mathbf{u}$, $\mathbf{v}$, $\mathbf{w}$ be the unit vectors in the coordinate frame defined by the telescope baselines, with $\mathbf{w}$ perpendicular to the uv-plane, which is itself parallel to the tangent plane on the sky. Let l, m and n be the direction cosines to $\mathbf{s}$ in the u, v, w coordinate system, i.e. $l = \mathbf{s} \cdot \mathbf{u}$, $m = \mathbf{s} \cdot \mathbf{v}$ and $n = \mathbf{s} \cdot \mathbf{w}$, and $l^2 + m^2 + n^2 = 1$. Then it can be shown that the visibilities, V, can be written as the 3D Fourier transform of the sky brightness I

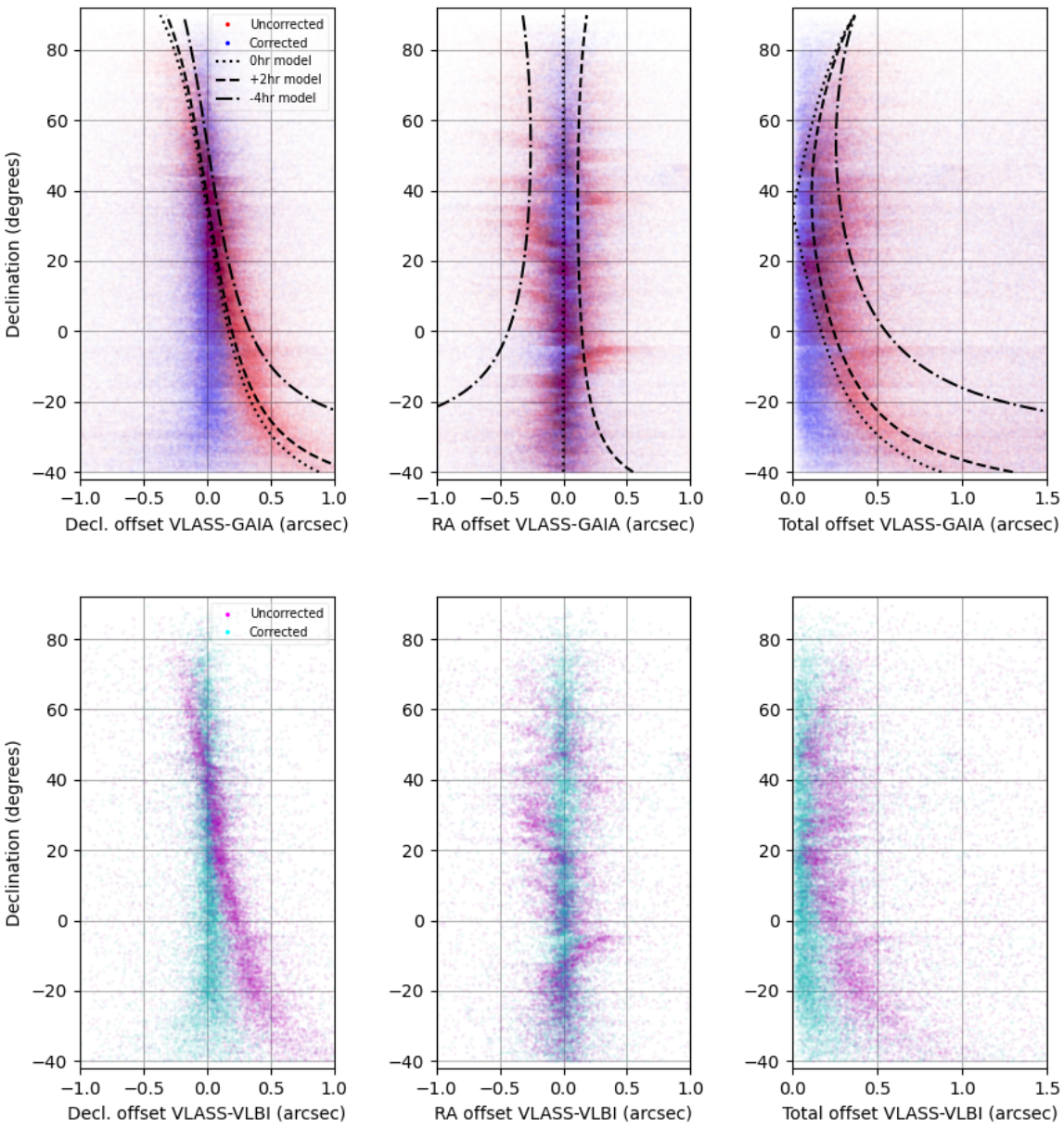

Figure 1: Position offsets in VLASS Quick Look mosaics. The upper row of plots shows the comparison to *Gaia* EDR3. The red points are the differences between VLASS and *Gaia* positions before the correction described in this Memo, the blue points the corrected positions. The lines are three simulations at different hour angles from Equations 6 and 7. The lower row of plots shows the comparison to VLBI positions. The magenta points are the differences between VLASS and VLBI positions before the correction described in this Memo, the cyan points the corrected positions.

and primary beam correction P (Cornwell & Perley 1992):

$$V(u,v,w) = \int\int I(l,m)P(l,m)\mathrm{e}^{-2\pi i(ul+vm+wn)}\frac{\mathrm{d}l\,\mathrm{d}m}{\sqrt{1-l^2-m^2}}. \quad (1)$$

(This is only a 2-D integral as it is constrained to the unit sphere, so $n = \sqrt{1-l^2-m^2}$.) If we define F as the 3D Fourier transform of the visibilities, then

$$F(l,m,n) = \int\int\int V(u,v,w)\mathrm{e}^{2\pi i(ul+vm+wn)}\mathrm{d}u\,\mathrm{d}v\,\mathrm{d}w. \quad (2)$$

The phase (equivalent to a position error if not corrected for) introduced by the w-term is thus $2\pi nw = 2\pi\sqrt{1-l^2-m^2}w \sim \pi(l^2+m^2)w$.

As pointed out by Cornwell & Perley (1992), the differing projection of the u,v plane across the primary beam is an important aspect of this analysis in the case of wide-field imaging. The scaling of the u,v axes is determined by the local tangent plane. For observations off zenith, the projected lengths of the baselines are foreshortened by an amount depending on the hour angle and declination of the phase center. The mosaicking algorithm (in the absence of w-term corrections) convolves each point in the uv plane by the Fourier transform of the antenna primary beam. Thus any point in the image plane can be thought of as comprising contributions from the sky image multiplied by the primary beam response. Points in the primary-beam-multiplied sky image that are farther from zenith will thus have a slightly differently-scaled uv-plane than those closer to zenith, resulting in a nonlinear scale variation of the coordinates across the primary beam, and a shift in the source position when the image is reconstructed.

The magnitude of this effect can be estimated by considering a source at transit observed at zenith distance ζ with a primary beam half-width of ϵ (Figure 2). The effect is related to the differing projections of the v axis at one edge of the primary beam, where the projected length of the v axis is proportional to $\cos(\zeta-\epsilon)$, to the other edge, where it is proportional to $\cos(\zeta+\epsilon)$, resulting in a net difference of apparent position for a source with a direction cosine $l = \cos(90-\epsilon) = \sin\epsilon$, $\Delta l \sim l\,(1/\cos(\zeta+\epsilon) - 1/\cos(\zeta-\epsilon)) \approx 2\,l\,\epsilon\tan\zeta/\cos\zeta$. If, for convenience, we assume a zenith distance of 24 deg. where $\tan\zeta/\cos\zeta = 0.5$, this rough calculation suggests the offset should be $\approx \epsilon^2$ radians, ≈ 1 arcsec for the VLA 3 GHz primary beam HWHM of 7.2 arcmin.

In the general case of an observation performed at a non-zero hour angle, both the u and v axes are differently foreshortened. The u,v axes rotate with the parallactic angle as the source moves away from transit, resulting in offsets in both RA and Dec. The RA offsets are approximately symmetric in hour angle either side of zenith (only approximately because the VLA north arm is slightly offset from N-S). In the particular case of an object transiting at zenith at the VLA (i.e. with $\delta = 34.1°$), the offset in declination is always positive. This explains why the trend of Declination offset with Declination does not pass through zero at 34.1° (Figure 1) - observations with the VLA cannot be made at the zenith, thus observations at $\delta = 34.1°$ always need to be offset from zero hour angle.

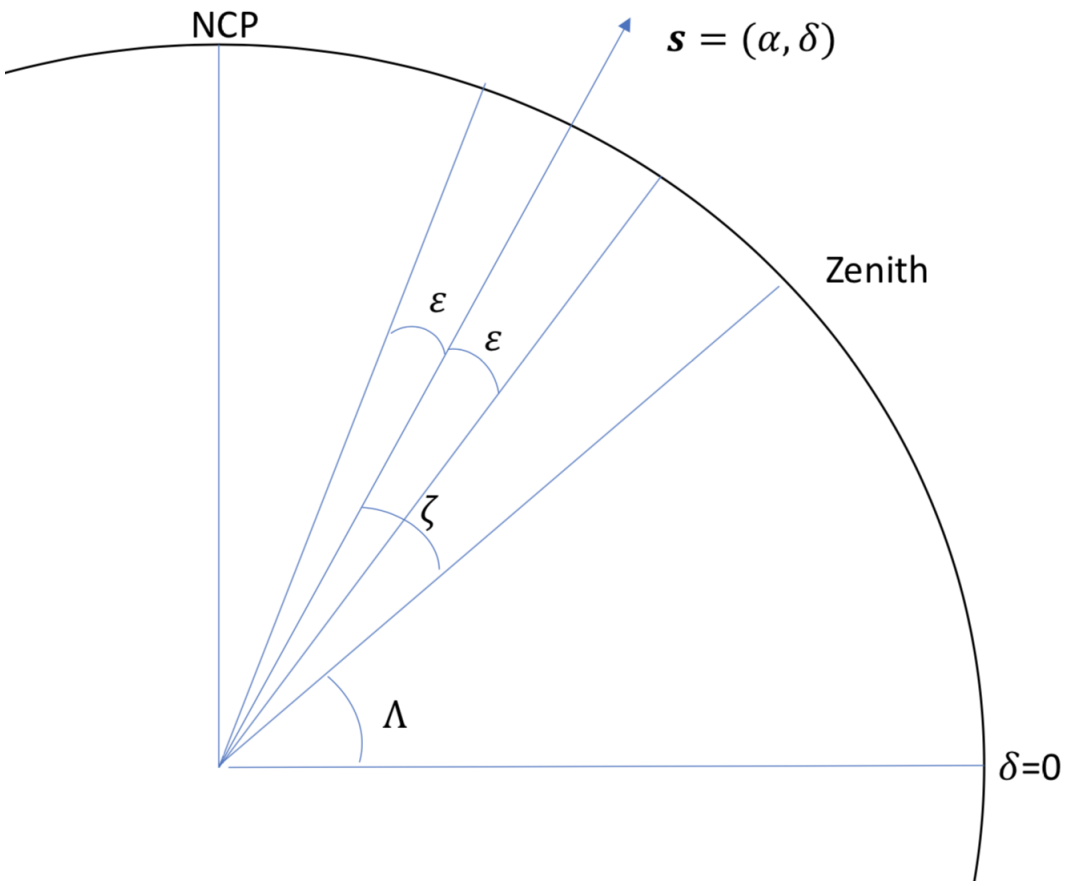

Figure 2: Geometry at transit, where an observation at vector $\mathbf{s}$ is observed at a zenith distance ζ with a primary beam HWHM of ϵ.

Mathematically, the analysis is as follows. Bracewell (1984) showed that, for any given instant in time, w can be eliminated from Equation (1) by rewriting it in terms of projected l and m values l' and m':

$$V(u,v,w) = \int\int I(l,m)P(l,m)\mathrm{e}^{-2\pi i(ul'+vm')}\frac{\mathrm{d}l\,\mathrm{d}m}{\sqrt{1-l^2-m^2}}. \quad (3)$$

Condon et al. (1998) (see also Cornwell, Golap & Bhatnagar 2008) give the relationship between l and m coordinates and the 2D projection, l' and m', in terms of the zenith distance, ζ, and the parallactic angle, χ: [1]

$$l' = l + \tan\zeta\,\sin\chi\,\left(\sqrt{1-l^2-m^2}-1\right) \quad (4)$$

$$m' = m + \tan\zeta\,\cos\chi\,\left(\sqrt{1-l^2-m^2}-1\right). \quad (5)$$

These distortion corrections can be directly applied in the image plane in the case of snapshot imaging, this was done for example in the NRAO VLA Sky Survey (NVSS; Condon et al. 1998) and the Faint Images of the Radio Sky at Twenty centimetres survey (FIRST; Becker, White and Helfand 1995). However, for an on-the-fly mosaic such as VLASS another approach is needed to avoid having to image each phase center separately and combine corrected images in the image plane.

Consider a source towards the edge of the primary beam, an angle ϵ from the phase center such that $\epsilon^2 = l^2 + m^2$ and $\epsilon^2 << 1$. Then, expanding up to 2nd order in ϵ,

$$l' - l \approx -\frac{\epsilon^2}{2}\tan\zeta\,\sin\chi \quad (6)$$

$$m' - m \approx -\frac{\epsilon^2}{2}\tan\zeta\,\cos\chi. \quad (7)$$

In practice, we can treat ϵ as a free parameter of order the primary beam width, as it is not clear exactly how the mosaicking will weight data from different parts of the primary beam, particularly for the wide bandwidth used by VLASS. Comparing to the analysis of tiles at extreme hour angle, H, and δ in Section 4 below, we find that $\epsilon \approx 5.4$ arcmin seems to be a good estimate. In Figure 1 we overplot this model on real and simulated data.

To correct for the wide-field imaging issues, the w-projection algorithm has been developed in CASA (Cornwell, Golap & Bhatnagar 2005). However, this is too computationally

[1] The parallactic angle is given by:

$$\chi = \arctan(\sin H/(\cos\delta\tan\Lambda - \sin\delta\cos H))$$

where H is the hour angle and Λ is the latitude of the telescope, and the zenith distance is:

$$\zeta = \arccos(\sin\Lambda\sin\delta + \cos\Lambda\cos\delta\cos H).$$

expensive for use with the Quick Look images, which need to be produced within a few weeks of observation, and, with the current gridder, it is also too slow for SE continuum images (the GPU-based gridder currently under development should improve the speed significantly).

3. Simulations

To help validate the analysis above, we constructed a set of 22 simulated observations using the CASA simulator. Accurately simulating the raster pattern of VLASS observing would be very time consuming, so instead we simulated an observation of a point source centered on a 3×3 grid of pointings separated by 7 arcmin in RA and Dec., observed over range of hour angle and declination (Table 1). These simulations sufficiently capture the visibilities contributing to each phase center. The simulated uv datasets were then imaged in CASA with the mosaic gridder and the source positions recovered with IMFIT and compared to the input positions. The predictions from the model of Section 2 agree fairly well with the measured offsets, though the predictions are typically below the measured value by $\approx 15\%$, suggesting that the value of ϵ chosen is a little small. As discussed in Section 4 though, unsimulated effects such as spillover may make the offsets at little smaller at high zenith distances/low elevations.

To study the variation of offset within a VLASS 1 deg^2 image, we constructed a second, larger large simulation with a 9×9 pointing grid, with points separated by 7.2 arcmin in RA and Dec, at δ =0.0 and transit, containing 25 sources on a 5×5 grid separated by 10 arcmin. The results showed that any variation of the offset across a 1 deg^2 image is small ($< 10\%$ of the average offset), and the offset is independent of the source position relative to the pointing or phase centers, as expected from the analysis above.

4. Correction algorithm for VLASS Quick Look images

VLASS is observed mostly in tiles of size 10×4 degrees, which take approximately 2 hr to execute, with a raster pattern of pointings that usually (though not always) runs from south to north. The scan direction is in R.A., and each row is separated by 7.2 arcmin. Thus there is significant hour angle variation within a single VLASS tile. Nevertheless, plotting the offsets of individual tiles can be used to provide a test of whether our model and simulations are approximately correct.

In order to correct the positions in VLASS Quick Look images, we wrote a script to apply the correction for the mean declination and mean hour angle of observation of the data that went into imaging that area of sky by changing the header reference coordinate values (CRVAL1, CRVAL2) values in each 1 deg^2 mosaic image. We split the tile observation into the four rows of 1 deg^2 images and apply a single correction per row appropriate for the mean H and δ for that row using Equations 6 and 7. There will inevitably be some

Simulation	Source Dec	HA (deg)	RA Offset (arcsec)	Dec Offset (arcsec)	Predicted RA offset (arcsec)	Predicted Dec offset (arcsec)
1.	-20:00:00	0	0.00	0.38	0	0.35
2.	-39:53:00	0	0.00	1.0	0	0.87
3.	+70:00:00	0	0.0	-0.21	0	-0.18
4.	+00:00:00	0	0.0	0.19	0	0.17
5.	+00:00:00	45	0.28	0.27	0.25	0.24
6.	+00:00:00	-45	-0.30	0.28	-0.25	0.24
7.	+34:06:00	30	0.13	+0.02	0.11	0.02
8.	+34:06:00	-30	-0.13	+0.02	-0.11	0.02
9.	+34:06:00	60	0.30	+0.10	0.27	0.09
10.	+34:06:00	-60	-0.30	+0.10	-0.27	0.09
11.	+45:00:00	0	0.0	-0.06	0	-0.05
12.	+45:00:00	45	0.21	-0.01	0.18	-0.01
13.	+45:00:00	-45	-0.19	-0.00	-0.18	-0.01
14.	+70:00:00	-45	-0.24	-0.14	-0.20	-0.12
15.	+70:00:00	45	0.23	-0.14	0.20	0.12
16.	-39:53:00	-30	-0.63	1.34	-0.54	1.17
17.	-39:53:00	30	0.61	1.33	0.54	1.17
18.	-20:00:00	-30	-0.24	0.43	-0.21	0.40
19.	-20:00:00	+30	0.23	0.44	0.21	0.40
20.	-39:53:00	-15	-0.24	1.06	-0.21	0.93
21.	-39:53:00	15	0.23	1.06	0.21	0.93
22.	+34:06:00	0	0.0	0.0	0	0

Table 1: Offsets in RA and Dec. measured for sources at the center of a 3×3 pointing grid, with a $7'$ grid spacing, compared to the predictions of the model.

Tile	$\Delta(\alpha)$ uncorrected (arcsec)	$\Delta(\delta)$ uncorrected (arcsec)	$\Delta(\alpha)$ corrected (arcsec)	$\Delta(\delta)$ corrected (arcsec)
T01t01	0.00	0.55	0.00	-0.22
T18t18	-0.31	0.13	-0.06	0.04
T09t12	0.15	0.24	0.01	0.06
T19t20	0.16	0.01	0.02	-0.01

Table 2: Effect of correction on the mean offsets in R.A. and Dec. with respect to the *Gaia* frame.

residual smearing from the hour angle range across the 1 deg. R.A. spread and the time range over which the strip was taken, but this should be $< 0\farcs1$.

We tested this correction on four VLASS1.1 tiles, including two tiles at the observational extremes, T18t18, a tile that transits near zenith, and was taken at $H \approx 3-4$ hr to avoid transit and the T01t01 tile in the far south at $\delta = -40$ to $\delta = -36$. The results are shown in Table 2 and Figure 3. The correction is not perfect: it slightly undercorrects the T18t18 tile in R.A. by $0\farcs06$, and slightly overcorrects T01t01 in Dec by $0\farcs22$, perhaps because the effective primary beam is not uniform with elevation due to spillover or exactly circular due to the OTF observing pattern. Nevertheless, the results indicated that we are able to correct the systematic offsets in about 90% of the survey to within $\approx 0\farcs1$ and all of the survey to within $\approx 0\farcs3$, 1/10th of the FWHM of the VLASS synthesized beam. We also included two more typical tiles, T09t12 and T19t20, whose results show that the correction works well in general even without further tuning.

5. Implementation of position corrections in the VLASS Quick Look and SE continuum pipelines

A per-image correction has been implemented in the VLASS CASA pipeline (version 5.6.3; tickets PIPE-587 and PIPE-700) to be applied to Quick Look and SE continuum images made using the mosaic gridder. This correction improves on the algorithm described above by using the actual RA, Dec of the image from the image header rather than the average RA, Dec. for the tile, but is otherwise the same as that described above. During testing, we found that care needed to be taken in the far Northern sky when the denominator of the fraction that is used to calculate χ passes through zero ($\tan\delta = \cos\lambda/\cos H$). At this δ, the solution for the χ, which is calculated as an inverse tangent, can switch from positive to negative values, causing the incorrect offset to be applied. A simple fix was implemented to prevent this by adding or subtracting π to maintain the same sign for χ as H.

The overall effectiveness of the correction for Quick Look images can be seen in Figures 1 and 4, with a quantitative comparison in Table 3. The correction reduces the mean offset between VLASS and VLBI coordinates over the entire declination range of the survey,

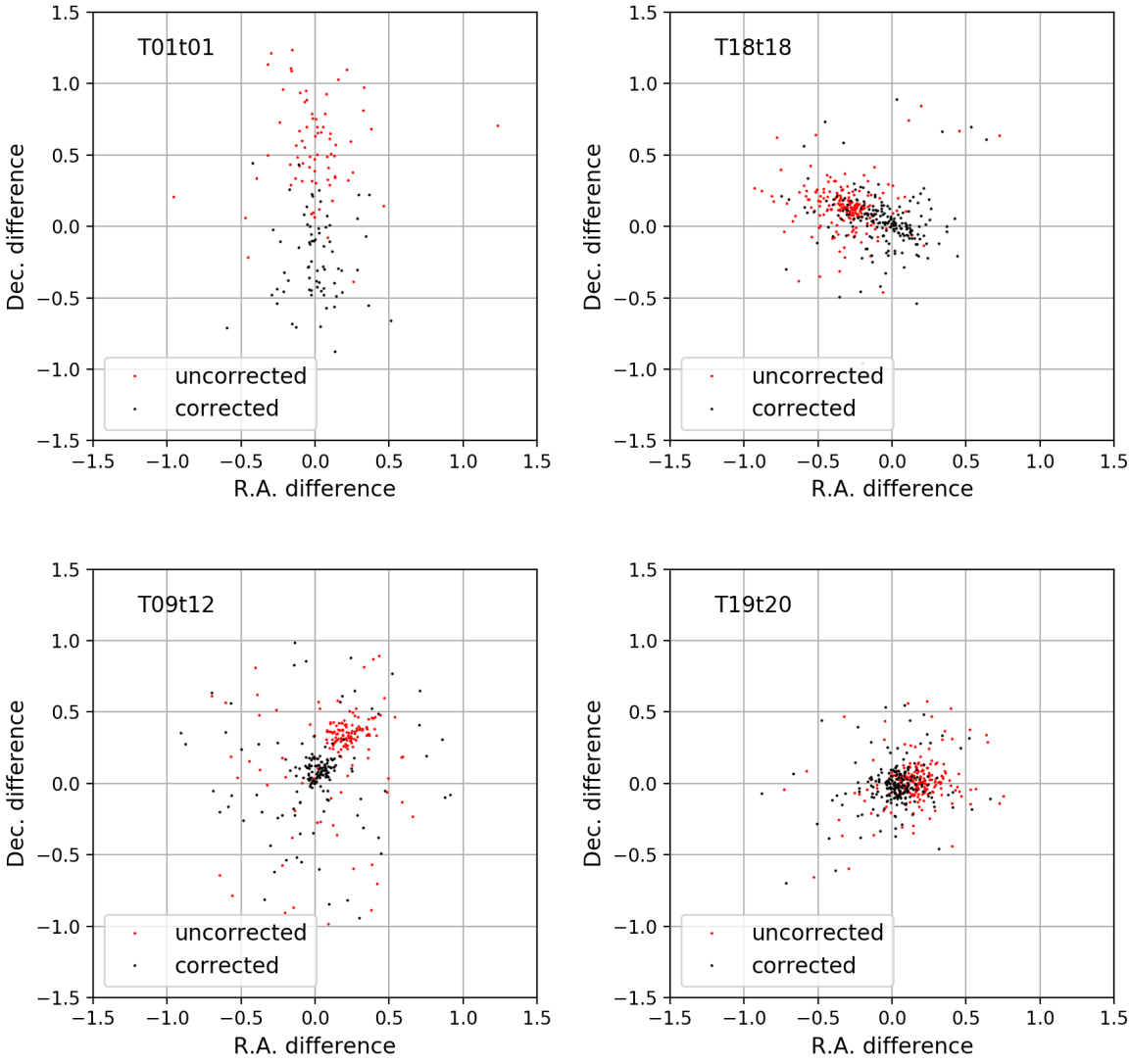

Figure 3: Effect of correction on the offsets in RA and Dec. with respect to the *Gaia* frame of the four VLASS tiles in Table 2.

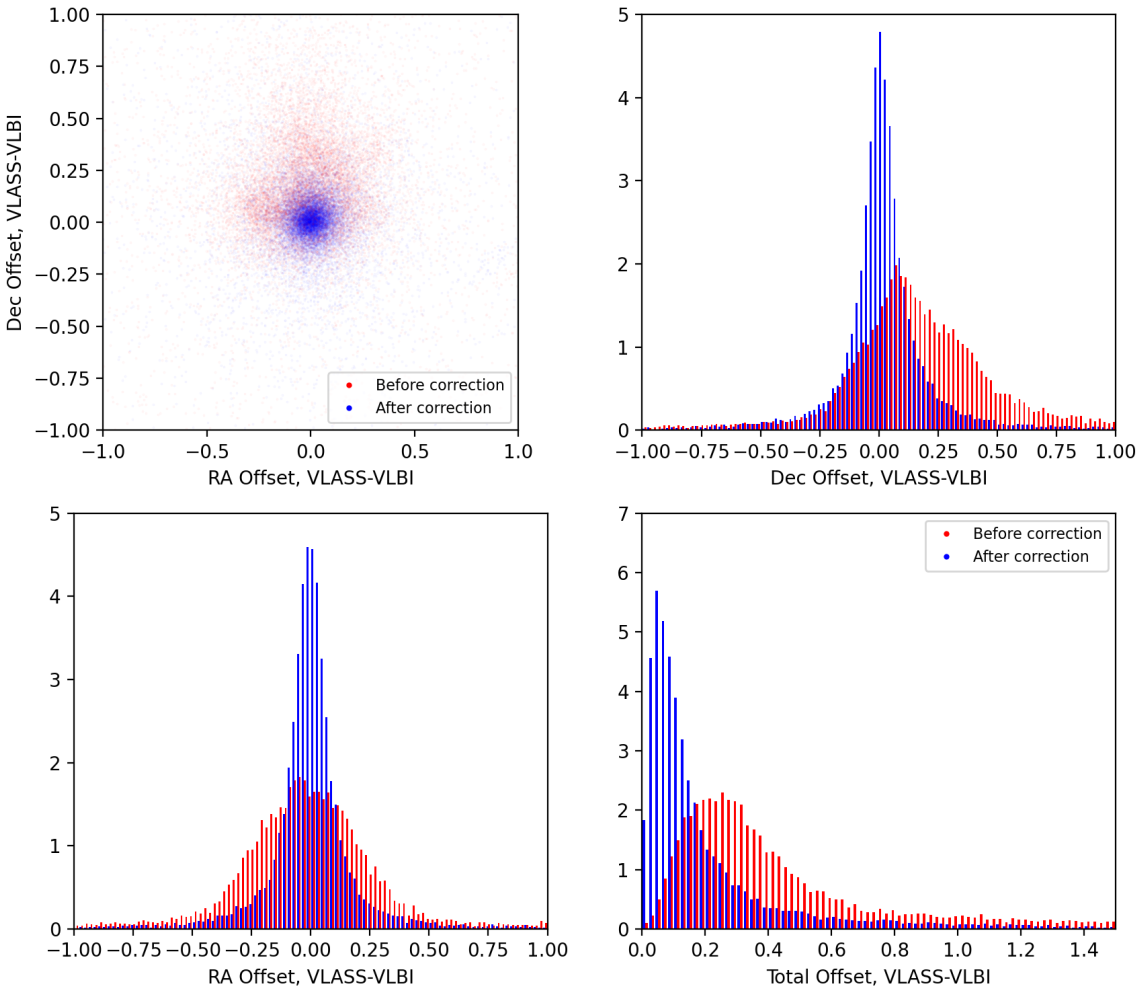

Figure 4: Offsets in VLASS1.2 and VLASS2.1 Quick Look with respect to VLBI before (red) and after (blue) correction.

Table 3: Position offsets and scatter in Quick Look relative to VLBI before and after correction, as a function of Declination.

Decl. range	Median offset (uncorrected) (arcsec)	Median offset (corrected) (arcsec)	Scaled MAD error (uncorrected) (arcsec)	Scaled MAD error (corrected) (arcsec)
-40 to -30	0.67	0.27	0.30	0.23
-30 to -20	0.48	0.16	0.18	0.12
-20 to -10	0.38	0.12	0.14	0.09
-10 to 0	0.37	0.09	0.18	0.11
0 to 10	0.25	0.09	0.11	0.07
10 to 20	0.20	0.08	0.12	0.07
20 to 30	0.23	0.10	0.13	0.08
30 to 40	0.28	0.10	0.14	0.09
40 to 50	0.22	0.11	0.15	0.10
50 to 60	0.14	0.10	0.22	0.08
60 to 70	0.30	0.10	0.16	0.08
70 to 80	0.19	0.13	0.38	0.10
80 to 90	0.59	0.17	0.40	0.14

and it also reduces the scatter about the mean. The positional accuracy over the survey is improved from a scatter (scaled mean absolute deviation) of 0.2 arcsec about a mean systematic offset of 0.3 arcsec to a scatter of 0.1 arcsec about a residual mean systematic offset of 0.1 arcsec. In the far south of the survey (Dec. $< -30^\circ$) the correction is less good, with a scatter of 0.2 arcsec about a mean offset of 0.3 arcsec, but this is much improved over the uncorrected data (scatter of 0.3 arcsec about a mean systematic offset of 0.7 arcsec).

6. The effects of wide bands and correcting the VLASS cubes

6.1. Dependence of the position offset on spectral index

The position correction derived in Section 2 is dependent on frequency, and will vary across a wide band, such as that in VLASS. From Equations (6) and (7) we can write the total offset $\Delta\theta$ as:

$$\Delta\theta = \frac{\epsilon^2}{2}\tan\zeta \tag{8}$$

where $\epsilon \approx 5.4$ arcmin at the effective band center. ϵ scales inversely with frequency, $\epsilon(\nu) = \epsilon_0\ (\nu_0/\nu)$, so:

$$\Delta\theta(\nu) = \frac{\epsilon_0^2}{2}\left(\frac{\nu_0}{\nu}\right)^2 \tan\zeta. \tag{9}$$

As the amplitude of the offset correction, ϵ, is calibrated using the ensemble source population, the effective mean frequency is a little offset from the 3 GHz center of the band.

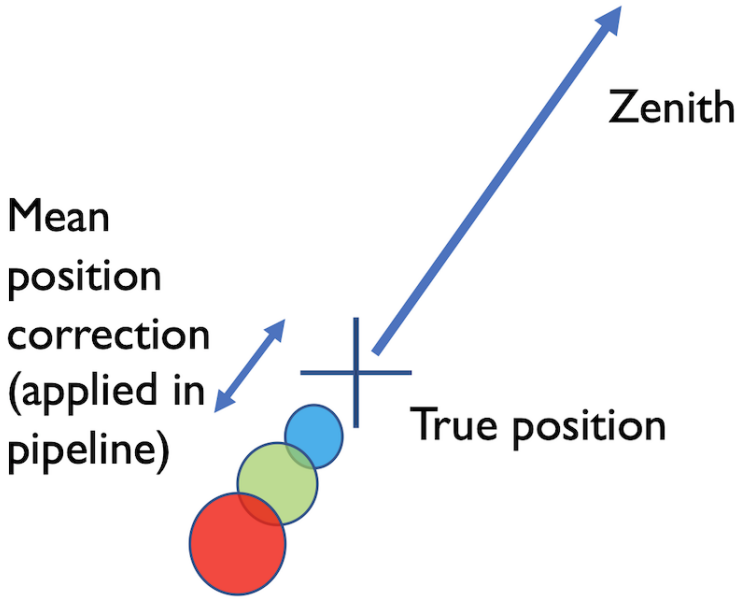

Figure 5: A sketch illustrating how the effects of the wide band on the position corrections lead to chromatic aberration in the wideband continuum images. The relative size of the offsets have been exagarrated for clarity.

Assuming a spectral index of α, where $S_\nu = S_0 \nu^{-\alpha}$,

$$\nu_{\rm eff} = \int_{\nu_1}^{\nu_2} S_0 \, \nu^{-\alpha} {\rm d}\nu = \frac{1-\alpha}{2-\alpha} \left(\frac{\nu_2^{2-\alpha} - \nu_1^{2-\alpha}}{\nu_2^{1-\alpha} - \nu_1^{1-\alpha}} \right) . \tag{10}$$

For a typical $\alpha = 0.8$, $\nu_{\rm eff} = 2.91$ GHz, and the position correction, inversely proportional to the square of the frequency, will differ from that for an object with $\alpha = 0$ by about 6%. We consider this negligible compared to the uncertainty in ϵ, but this effect should be borne in mind for objects with extremely steep or extremely inverted spectra.

6.2. Chromatic aberration effects

The frequency dependence of the position offset will introduce a smearing effect analogous to chromatic aberration in optical systems due to the differing offset for each frequency contributing to the *tt*0 image (Figure 5). Simulations suggest that this is small, ≈2% of the peak beam value at $\zeta = 65°$ (Figure 6).

A more significant implication of frequency-dependent effects is apparent in the in-band

spectral index estimates. The $tt1$ image is effectively a difference image across the band:

$$tt1 = \int_{\nu_1}^{\nu_2} \frac{S_\nu - S_{\nu_0}}{\nu - \nu_0} \mathrm{d}\nu \tag{11}$$

so, as the beam at one edge of the band is differently displaced from that at the other, the $tt1$ image will show a dipole-like distortion. This leads to spectral indices derived from the mosaic gridder (especially with conjbeams=False) to become less accurate than the survey requirement of $\Delta\alpha = 0.2$ for $\zeta \gtrsim 45°$ (Figure 6).

6.3. Correction of the VLASS cubes

We propose a per-plane correction of the VLASS cubes using Equation 9. This should remove the chromatic aberration effects described above for the cubes, and allow us to use the mosaic gridder over the whole sky.

We tested this by applying the correction to each plane, then running imregrid to re-sample each cube plane back to the original projection, for ease of analysis (otherwise each plane's WCS is offset by a small, typically subpixel, amount). We confirm that even the small relative offsets between the cube planes, if not corrected as described above, can produce significant errors ($\sim 0.1 - 0.2$) in the spectral index across a source.

7. Summary

We illustrate the need for proper treatment of the wide-field terms to produce accurate positions in wide field mosaic images. We show that the position offsets observed in mosaics when wide-field corrections are ignored are a purely geometric effect, dependent only on the hour angle and declination of the observation and the primary beam size. The effect scales with the square of the primary beam size, so is thus most noticeable at lower frequencies in the larger array configurations; however, we note that for applications requiring high precision astrometry from mosaics, w-term corrections should always be used. Correct treatment of the wide-field terms is computationally expensive, however, and we show that the offsets can be reliably modeled. We described a post-processing correction in the image plane that can correct positions in VLASS Quick Look images to within 1/10th of the synthesized beam width (0.3 arcsec) that has now been implemented in the VLASS Quick Look and SE pipelines. Wideband data needs to be treated with care as the positional offsets are a function of the square of the wavelength. We show that, while the effects on the tt0 image is small, the effect on the tt1 image (and spectral index) can be significant. We recommend that the cube imaging pipeline employ a frequency dependent position correction to correctly align sources through the cube planes to allow a good reconstruction of the intrinsic spectral index.

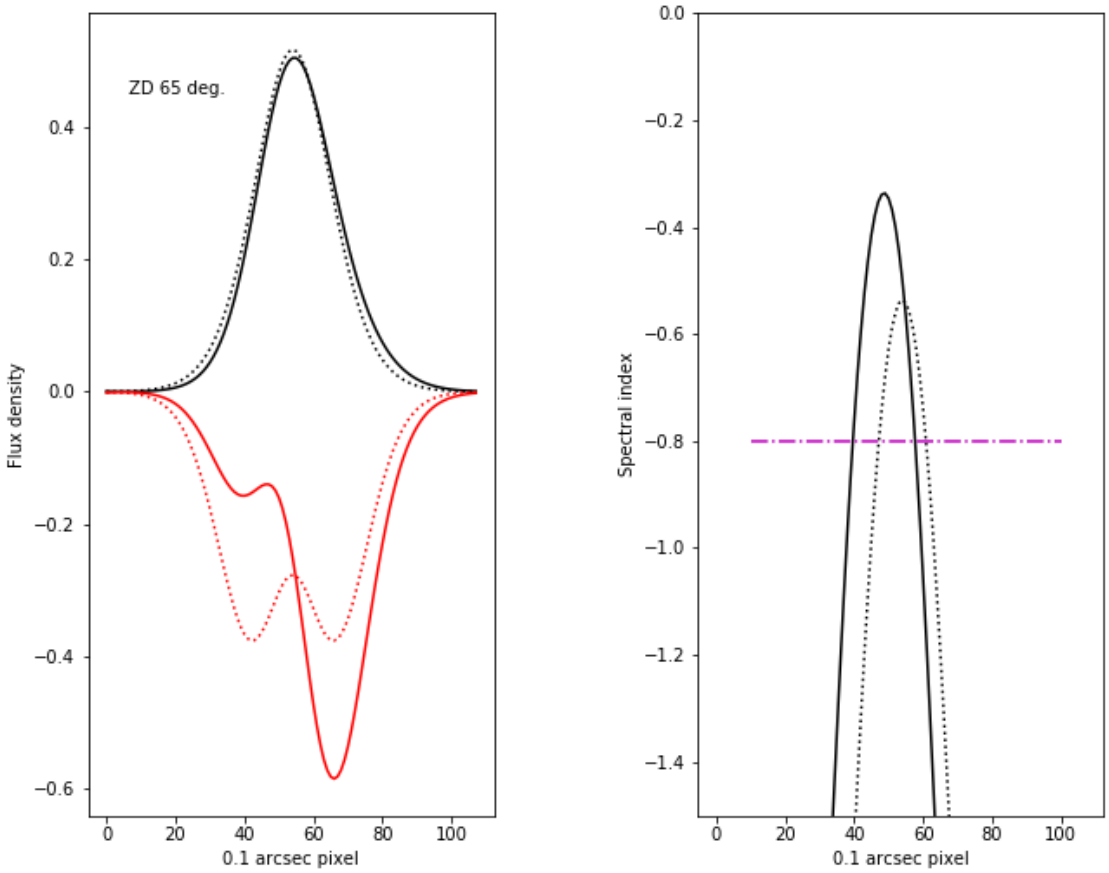

Figure 6: Simulated beam and beam ratio cross-sections for an observation at a Zenith distance of 65° and a spectral index of -0.8. The beams use 0.1-arcsec pixels and are centered on pixel 55 in the simulation. tt0 and tt1 beam models were constructed by combining Gaussians for each of the 16 VLASS spectral windows (approximating the conjbeams=False approach by averaging the 16 beams to create the tt0 beam and using the discrete version of Equation 11 for the tt1 beam). Dashed lines show the beams in the case of fully-corrected w-terms (i.e. no shift between frequencies), solid lines uncorrected beams. In the left-hand plot the tt0 beam is shown in black, and the tt1 in red. In the right-hand plot, the spectral index estimate from ratioing the tt1 and tt0 beams is shown. Note that (1) the peak depression in tt0 from neglecting the w-term correction is small ($\approx 2\%$ in this case), and (2) even in the case of no w-terms, the recovered spectral index differs slightly due to the change in beam size with frequency (the conjbeams=True approach fixes this by applying the frequency-conjugate beam). The magenta dot-dashed line shows the input spectral index of -0.8.

Acknowledgment

This work has made use of data from the European Space Agency (ESA) mission *Gaia* (`https://www.cosmos.esa.int/gaia`), processed by the *Gaia* Data Processing and Analysis Consortium (DPAC, `https://www.cosmos.esa.int/web/gaia/dpac/consortium`). Funding for the DPAC has been provided by national institutions, in particular the institutions participating in the *Gaia* Multilateral Agreement.

8. References

Becker, R.H., White R.L & Helfand D.J. 1995, ApJ, 450,559
Bracewell, R. N. 1984, Indirect Imaging. Measurement and Processing for Indirect Imaging, Proceedings of an International Symposium held in Sydney, Australia, August 30-September 2, 1983. Ed. J.A. Roberts. Cambridge University Press. LC # QB51.3.E43 I53 1984. ISBN # 0-521-26282-8. P.177
Condon, J. J., Cotton, W. D., Greisen, E. W., et al. 1998, The Astronomical Journal, 115, 1693
Cornwell, T.J. & Perley, R.A. 1992, A&A, 261, 353
Cornwell, T. J., Golap, K., & Bhatnagar, S. 2005, Astronomical Data Analysis Software and Systems XIV, 86
Cornwell, T. J., Golap, K., & Bhatnagar, S. 2008, IEEE Journal of Selected Topics in Signal Processing, 2, 647
Gaia Collaboration et al. 2016, A&A 595, A1
Gaia Collaboration et al. 2020 arXiv:2012.01533
Kovalev, Y. Y., Petrov, L., & Plavin, A. V. 2017, A&A, 598, L1
Petrov, L. et al. 2021, AJ, 161, 14